Journal of Materials Chemistry B

ROYAL SOCIETY OF CHEMISTRY

PAPER

View Article Online
View Journal | View Issue

Cite this: J. Mater. Chem. B, 2025, 13, 13282

Glassy organic dots exhibiting near-infrared TADF with quantum yields >40% for cellular imaging

Xujun Qiu,†[a] André Jung,†[b] Angelica Sevilla-Pym,†[a] Peiqi Hu,[a] Stefan Bräse*[bc] and Zachary M. Hudson*[a]

Received 28th July 2025,
Accepted 17th September 2025

DOI: 10.1039/d5tb01740h

rsc.li/materials-b

Near-infrared (NIR) thermally activated delayed fluorescence (TADF) imaging integrates the benefits of both NIR emission and TADF mechanisms, offering enhanced sensitivity and deeper tissue penetration while enabling time-resolved imaging for biological and medical applications. In this study, we synthesized and studied a donor–acceptor (D–A) type TADF emitter, 7,8-bis(4-(di([1,1′-biphenyl]-4-yl)amino)phenyl)phenazine-2,3-dicarbonitrile (**DPPZ**), which exhibits strong NIR fluorescence. The photophysical properties of **DPPZ** were characterized in both toluene and poly(methyl methacrylate) (PMMA) films. In degassed toluene, **DPPZ** displayed a maximum emission peak at 724 nm with a high photoluminescence quantum yield (Φ_{PL}) of 54.4%, while maintaining a Φ_{PL} of 43.9% in PMMA film under aerated conditions. Upon encapsulation into glassy organic dots (g-Odots), the emitter retained its NIR emission, a Φ_{PL} of 40.1%, and a notably long delayed lifetime (τ_d) of up to 225.5 μs. These NIR-emissive g-Odots were subsequently applied for lysosome-targeted bioimaging in HeLa cells, demonstrating their potential as effective probes for subcellular imaging.

Introduction

Thermally activated delayed fluorescence (TADF) materials have garnered considerable attention in recent years for their promising applications in advanced fluorescence imaging.[1–8] Originally popularized for optoelectronic applications by Adachi and coworkers,[9] they possess a unique capability to harvest both singlet and triplet excitons through rapid interconversion between the lowest singlet (S_1) and triplet (T_1) excited states facilitated by a small singlet–triplet energy gap (ΔE_{ST}). This enables reverse intersystem crossing (RISC) from T_1 to S_1 at room temperature, and can enable efficient electroluminescence by harvesting both singlet and triplet excitons.[10,11] Unlike conventional fluorophores, which emit fluorescence on the nanosecond timescale, TADF materials typically exhibit both short (ps-ns) and long (μs-ms) emission lifetimes. The delayed fluorescence allows for time-resolved fluorescence imaging (TRFI), a powerful technique that temporally separates the long-lived emission of the probe from the short-lived autofluorescence of biological tissue by applying a brief delay to detector activation following a pulsed excitation. As a result, TRFI improves the signal-to-background ratio significantly and supports advanced imaging techniques such as multiplexed imaging, where multiple fluorophores can be distinguished based on their lifetime, spectral characteristics, or both.[12–16]

When TADF fluorophores emit in the near-infrared (NIR) spectral region (typically 650–1350 nm), they offer additional benefits for biological imaging.[17,18] NIR light experiences reduced light scattering and minimal absorption by biological tissues, leading to deeper tissue penetration and minimized background interference. These advantages make NIR TADF emitters particularly attractive for non-invasive, *in vivo* bioimaging applications.[19–24] Despite their advantageous photophysical properties, a major limitation of π-conjugated TADF dyes for biological applications is their intrinsic hydrophobicity. Most high-performance TADF emitters exhibit poor solubility in aqueous environments and suffer from aggregation-caused quenching, which significantly reduces their fluorescence intensity and limits their bioimaging utility.[25]

To address these challenges, glassy organic dots (g-Odots) have emerged as a versatile and effective platform for encapsulating hydrophobic TADF dyes.[26,27] g-Odots are water-dispersible nanoparticles composed of a hydrophobic host material, *e.g.* 1,3-bis(*N*-carbazolyl)benzene (mCP), a fluorescent TADF emitter, and an amphiphilic surfactant. These components spontaneously self-assemble through noncovalent interactions and are heated above the melting point of mCP. Upon rapid cooling, the mCP solidifies into a rigid, glassy matrix that

[a] Department of Chemistry, The University of British Columbia, 2036 Main Mall, Vancouver, British Columbia, V6T 1Z1, Canada. E-mail: zhudson@chem.ubc.ca; Fax: +1-604-822-2847; Tel: +1-604-822-3266
[b] Institute of Biological and Chemical Systems-Functional Molecular Systems, Karlsruhe Institute of Technology, Kaiserstrasse 12, 76131 Karlsruhe, Germany
[c] Institute of Organic Chemistry, Karlsruhe Institute of Technology, Kaiserstrasse 12, 76131 Karlsruhe, Germany. E-mail: braese@kit.edu; Fax: +49 721 608-48581; Tel: +49 721 608-42903
† These authors contributed equally to this work.

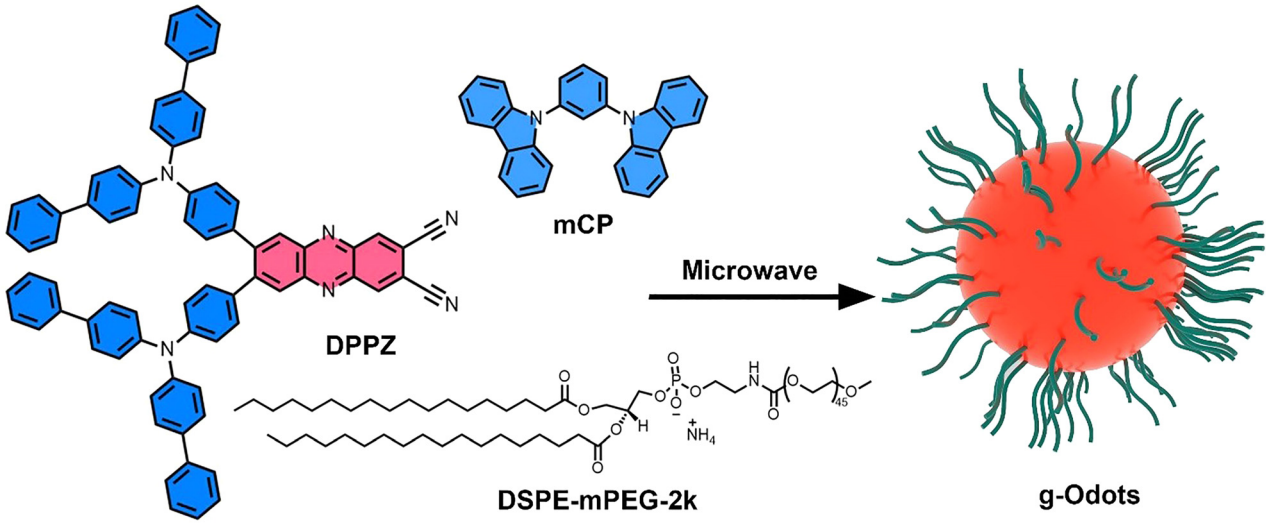

Scheme 1 Schematic illustration of microwave assisted synthesis of NIR g-Odots containing **DPPZ**.

enhances the stability and photophysical performance of the encapsulated dyes.[26]

The rigid interior of g-Odots protects the TADF emitter from oxygen quenching and restricts non-radiative decay, leading to increased Φ_{PL} and prolonged emission lifetimes. Moreover, g-Odots do not require chemical modification of the fluorophore, making them highly adaptable for integrating a wide variety of hydrophobic NIR TADF dyes into bioimaging platforms.[28–31] Unfortunately, however, NIR TADF dyes frequently suffer from low PLQYs due to the energy gap law, with all NIR g-Odots reported to date having PLQYs of 1–38%.[30,31] To improve the practicality of this technology, there is a need for NIR TADF probes with higher PLQYs to enable bioimaging with high signal-to-noise ratios.

In this study, we present a donor–acceptor (D–A) type TADF emitter, 7,8-bis(4-(di([1,1′-biphenyl]-4-yl)amino)phenyl)phenazine-2,3-dicarbonitrile (**DPPZ**) (Scheme 1), based on the previously reported phenazine-2,3-dicarbonitrile (PZ) acceptor,[32] engineered to exhibit strong NIR fluorescence for advanced bioimaging applications. The photophysical properties of **DPPZ** were thoroughly investigated in both degassed toluene solution and poly(methyl methacrylate) (PMMA) film. In toluene, **DPPZ** exhibited a maximum emission peak at 724 nm and achieved a high Φ_{PL} of 54.4% in a degassed solution and 45.6% in an aerated solution. Furthermore, it retained a Φ_{PL} of 43.9% in a PMMA matrix under air, confirming its solid-state emissive performance. To further improve its aqueous compatibility and stability, **DPPZ** was encapsulated into g-Odots, known for their enhanced photostability and rigidity. The resulting NIR g-Odots largely preserved the emission properties of the free emitter, exhibiting a blue-shifted peak at 694 nm and a Φ_{PL} of 40.1%, along with a prolonged delayed fluorescence lifetime (τ_d) of up to 225.5 μs, a beneficial feature for TRFI. The biocompatibility and functionality of these g-Odots were validated through lysosome-targeted imaging in HeLa cells, where they demonstrated efficient cellular uptake and selective subcellular localization, highlighting their potential as high-performance NIR probes for precise cellular imaging. Therefore, this work demonstrates that TADF architectures, originally designed for optoelectronic applications, can be successfully adapted for use in the biological field, yielding the highest PLQY reported to date for a NIR g-Odot.

Results and discussion

Synthetic procedures

The synthesis of **DPPZ** is shown in Scheme S1. The acceptor intermediate 7,8-dibromophenazine-2,3-dicarbonitrile was obtained by oxidation of 4,5-dibromobenzene-1,2-diol to form 4,5-dibromo cyclohexa-3,5-diene-1,2-dione, followed by condensation with 4,5-diaminophthalonitrile.[32] Subsequent palladium-catalyzed Suzuki–Miyaura cross-coupling gave **DPPZ** in 63% yield. The final product was fully characterized by ^{1}H NMR, ^{13}C NMR spectroscopy (Fig. S1 and S2), high-resolution ESI mass spectrometry and infrared (IR) spectroscopy.

Photophysical and electrochemical characterization

The photophysical properties of **DPPZ** were first studied in toluene solution (Fig. 1a). **DPPZ** exhibits two prominent absorption bands centered at 350 nm and 562 nm, which correspond to localized π–π* transitions of the conjugated backbone and an intramolecular charge transfer transition, respectively. In the photoluminescence spectrum, **DPPZ** shows a strong NIR emission peak at 724 nm. Upon increasing the solvent polarity, a slight bathochromic shift in the absorption edge is observed (Fig. 1b), accompanied by significant solvatochromic behavior in the emission spectra. These findings highlight the charge-transfer character of the S_1 state.

In degassed toluene, **DPPZ** exhibits a high Φ_{PL} of 54.4%, which decreases to 45.6% under aerated conditions (Fig. 1c). The prompt fluorescence lifetime (τ_p) was measured to be 10.0 ns in degassed solution and decreased to 6.34 ns upon

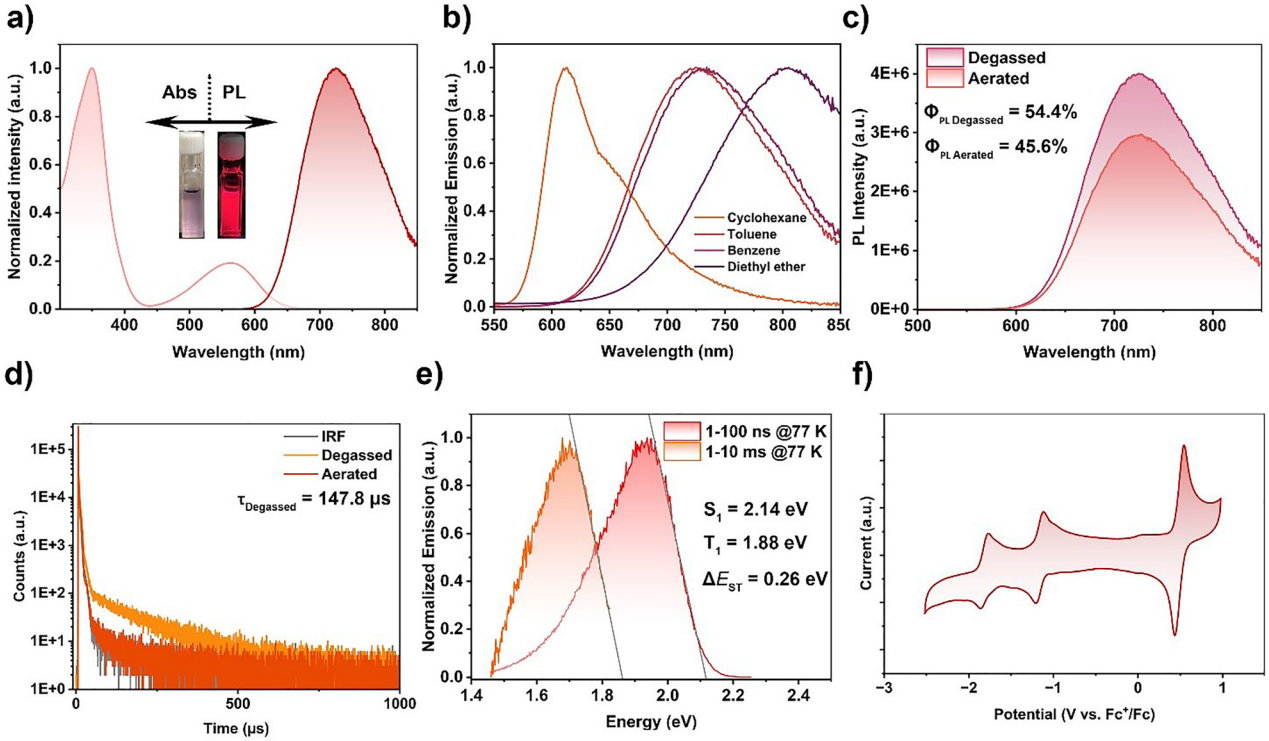

Fig. 1 (a) UV–vis absorption and PL spectra of **DPPZ** in toluene at room temperature (λ_{exc} = 380 nm, 1.0 × 10^{-5} M); (b) PL spectra of **DPPZ** in solvents of varying polarity (λ_{exc} = 380 nm, 1.0 × 10^{-5} M); (c) PL spectra of **DPPZ** in degassed and aerated toluene (λ_{exc} = 380 nm, 1.0 × 10^{-5} M); (d) time-resolved PL decay spectra of **DPPZ** in degassed and aerated toluene (λ_{exc} = 380 nm, 1.0 × 10^{-5} M); (e) prompt fluorescence (1–100 ns) and phosphorescence spectra (1–10 ms) recorded in toluene at 77 K of **DPPZ** (λ_{exc} = 380 nm, 1.0 × 10^{-5} M); (f) cyclic voltammograms of **DPPZ** recorded *versus* Fc/Fc^+ at 298 K in *o*-difluorobenzene under N_2 atmosphere.

aeration (Fig. S3), indicating energy transfer from the singlet excited state to oxygen. Additionally, a delayed fluorescence component (τ_d) with a lifetime of 147.8 µs was recorded in degassed toluene, but it was quenched significantly under aerated conditions (Fig. 1d). This pronounced oxygen sensitivity supports the involvement of a triplet excited state in the measured delayed fluorescence at room temperature, suggesting a TADF mechanism.

To further elucidate the excited-state energetics, prompt fluorescence and phosphorescence spectra of **DPPZ** were collected in toluene at 77 K. The onset of the spectra allowed estimation of the singlet (S_1) and triplet (T_1) energy levels, determined to be 2.14 eV and 1.88 eV, respectively, corresponding to a singlet–triplet energy gap (ΔE_{ST}) of 0.26 eV (Fig. 1e). This relatively small ΔE_{ST} is consistent with efficient RISC, characteristic of TADF-active compounds (Table 1).

Cyclic voltammetry (CV) was performed to examine the redox behaviour and estimate the frontier molecular orbital energy levels of **DPPZ**. As shown in Fig. 1f, the compound exhibited a reversible two-electron reduction process, attributed to the phenazine-2,3-dicarbonitrile acceptor moiety. In contrast, the reversible oxidation event is ascribed to the electron-donating triarylamine units. Based on the half-wave potentials ($E_{1/2}$) of the oxidation and reduction processes, the HOMO and LUMO energy levels were calculated to be –5.29 eV and –3.64 eV, respectively, comparable to literature values for structurally similar compounds.[32] Furthermore, CV measurements conducted at varying scan rates confirmed the electrochemical reversibility of both redox processes, as shown in Fig. S4.

The photophysical properties of **DPPZ** in the solid state were further investigated by doping the emitter into PMMA films at

Table 1 Summary of photophysical properties of **DPPZ**

Entry	λ_{abs} (nm)	λ_{em} (nm)	τ_p (ns)	τ_d (µs)	Φ_{PL} (%)	S_1/T_1 (eV)	ΔE_{ST} (eV)	$k_{ISC}/\times 10^8\ s^{-1}$[c]	$k_{RISC}/\times 10^4\ s^{-1}$[c]	$E_{HOMO/LUMO}$ (eV)	E_g (eV)
DPPZ	350, 562	724[a] [707][b]	6.34 (10.0)[a] [9.82][b]	n.d. (147.8)[a] [208.3][b]	45.6 (54.4)[a] [43.9][b]	2.14/1.8[a] [2.09/1.89][b]	0.26[a] [0.20][b]	1.1	2.0	−5.29/−3.64[a]	1.64[a]

[a] In toluene at 298 K (λ_{exc} = 380 nm). Values quoted are measured in air and values in parentheses are measured under N_2, n.d.= not detected. [b] Spin-coated 1 wt% emitters doped in PMMA films. S_1 was obtained from the onset of the prompt emission (time-gated window: 1–100 ns) measured at 77 K and T_1 was obtained from the onset of the phosphorescence spectrum (time-gated window: 1–10 ms) at 77 K. [c] In toluene, k_{ISC} = intersystem crossing rate constant; k_{RISC} = reverse intersystem crossing rate constant.[33]

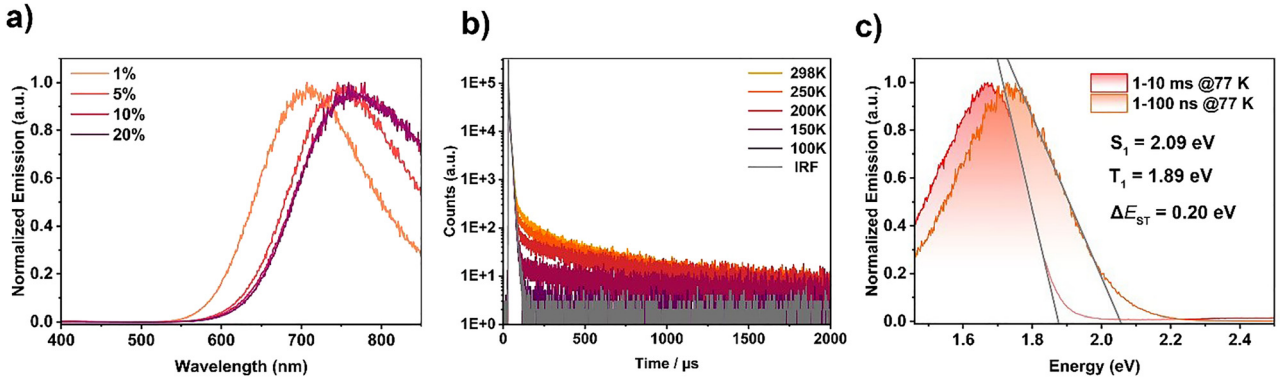

Fig. 2 (a) PL spectra of **DPPZ** in PMMA films at various doping concentrations at room temperature (λ_{exc} = 380 nm); (b) temperature-dependent time-resolved PL decay of 1 wt% doped films of **DPPZ** in PMMA (λ_{exc} = 380 nm); (c) prompt fluorescence (1–100 ns) and phosphorescence spectra (1–10 ms) of **DPPZ** in 1 wt% PMMA film at 77 K.

varying weight concentrations. As shown in Fig. 2a, increasing the doping concentration from 1 to 20 wt% led to a pronounced redshift in the PL emission, shifting from 707 nm at 1 wt% to 765 nm at 20 wt%, corresponding to a redshift of approximately 58 nm. This shift is likely due to the formation of emissive aggregates at higher doping levels. Concurrently, the Φ_{PL} decreased significantly with increasing concentration: 43.9% at 1 wt%, 24.6% at 5 wt%, 8.75% at 10 wt%, and 4.3% at 15 wt%, indicating strong concentration quenching. Based on these observations, subsequent photophysical characterizations were carried out using the 1 wt% doped PMMA film.

As shown in Fig. 2b and Fig. S5, the time-resolved PL measurements of **DPPZ** in the PMMA film revealed multi-exponential decay behavior with suppression of delayed fluorescence upon cooling from 298 to 100 K, indicative of TADF. At room temperature, the average τ_p was measured to be 9.82 ns, while the average τ_d reached 208.3 μs. The S_1 and T_1 energy levels were determined from the onset of the corresponding prompt fluorescence and phosphorescence spectra recorded at 77 K. These measurements yielded S_1 and T_1 energies of 2.09 eV and 1.89 eV, respectively, corresponding to a singlet–triplet energy gap (ΔE_{ST}) of 0.20 eV (Fig. 2c).

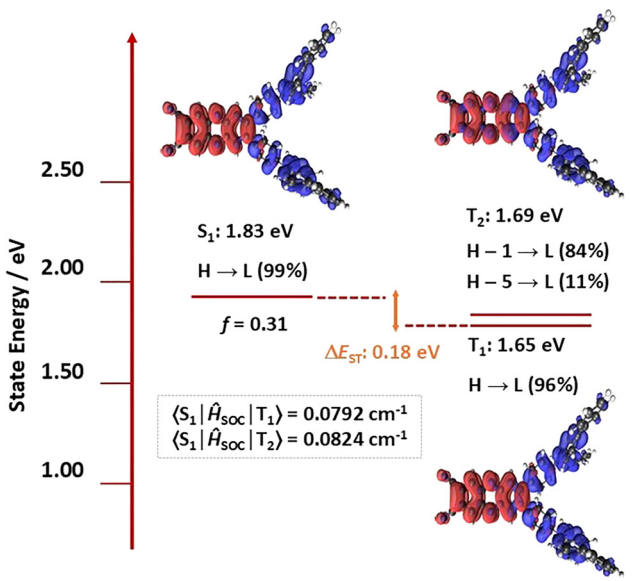

Fig. 3 Excited state energy levels of the first excited singlet (S_1) and the first two excited triplet states (T_1, T_2) incl. S_1 oscillator strength, natural transition orbitals (NTOs) and selected spin–orbit coupling constants; calculated at the (TD-)DFT PBE0/6-31G(d,p) level of theory in gas phase. Blue colour shows areas of decreasing electron density, red colour equals areas of increasing electron density during the transition.

Theoretical calculations

To predict and rationalize the electronic structure and excited states of **DPPZ**, density functional theory (DFT) and time-dependent DFT (TD-DFT) modelling were performed in the gas phase at the PBE0/6-31G(d,p) level. The calculated energy levels of the highest occupied molecular orbital (HOMO) and lowest unoccupied molecular orbital (LUMO) are presented in Fig. S6. The density distributions of HOMO and LUMO show adequate spatial separation. The LUMO is localized on the electron-withdrawing moiety, phenazine-2,3-dicarbonitrile, and has an energy level of −3.19 eV, while the HOMO is predominantly localized on the triphenylamine units at an energy level of −5.37 eV. This results in a calculated energy gap (ΔE) of 2.18 eV.

As shown in Fig. 3, the natural transition orbitals (NTOs) of the S_1, T_1, and T_2 excited states indicate predominant intramolecular charge transfer character. Notably, the NTOs of the S_1 state show a certain degree of overlap on the phenazine core at the junction points between the donors, contributing to a relatively high oscillator strength (f) of 0.31 for the S_0–S_1 vertical transition. Moreover, both T_1 and T_2 states are energetically close to the S_1 state ($\Delta E_{S_1T_1}$ = 0.18 eV, $\Delta E_{S_1T_2}$ = 0.14 eV) with similar spin orbit coupling constants between S_1–T_1 (0.0792 cm^{-1}) and S_1–T_2 (0.0824 cm^{-1}), suggesting the potential for multiple RISC channels.

g-Odot characterization and cellular imaging

Owing to the excellent photophysical properties in the NIR region, **DPPZ** demonstrated strong potential for bioimaging applications. To facilitate its use in biological environments,

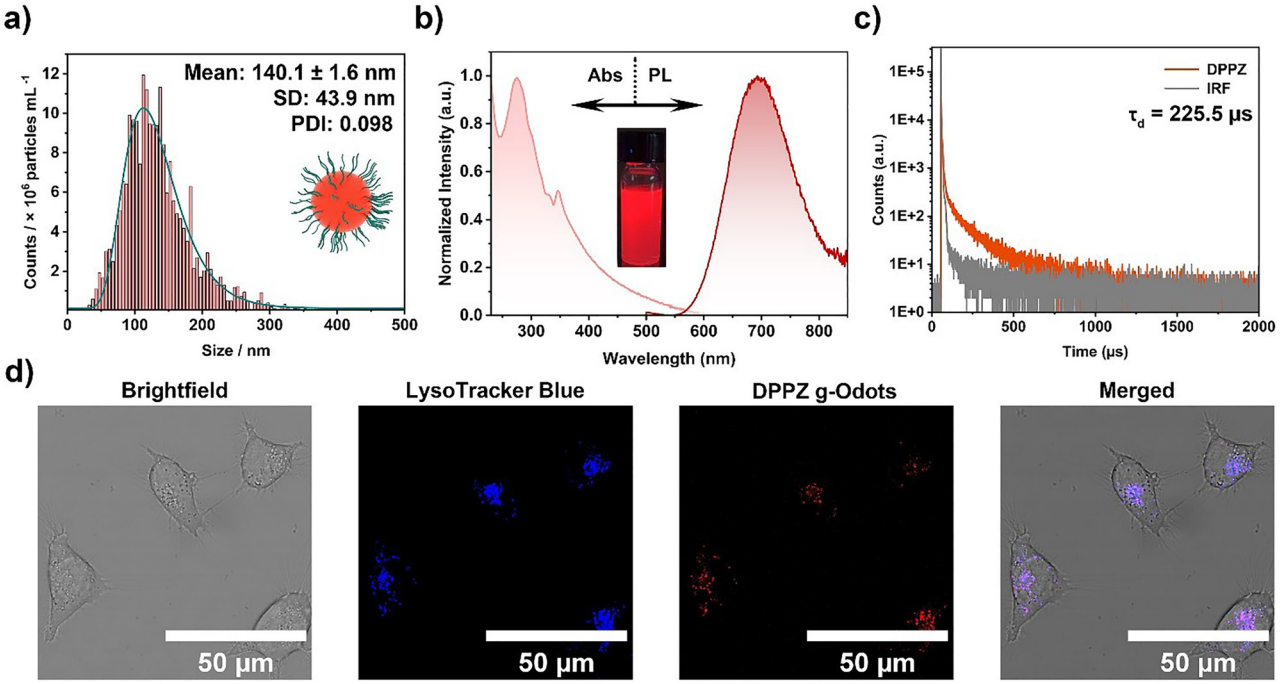

Fig. 4 (a) Size distribution of g-Odots doped with **DPPZ** obtained by NTA, fitted with a log-normal distribution, (b) PL spectra of g-Odots in water (λ_{exc} = 380 nm). Inset: photograph of g-Odot solution under 365 nm UV light; (c) PL decay of **DPPZ** doped g-Odots (λ_{exc} = 380 nm) in water at room temperature; (d) confocal fluorescence images of HeLa cells co-incubated for 2 h with **DPPZ** g-Odots and LysoTracker Blue DND-22, acquired with a 63× objective lens (λ_{exc} = 405 nm for LysoTracker and 561 nm for **DPPZ** g-Odots, respectively).

water-dispersible nanoparticles, referred to as glassy organic dots (g-Odots), were fabricated by co-encapsulating **DPPZ** and the small-molecule host mCP with the amphiphilic polymer DSPE-PEG2k. The g-Odots were prepared *via* a rapid emulsion-based method by heating an oil-in-water mixture containing mCP and DSPE-PEG2k (in a 5 : 1 molar ratio) with 1 wt% **DPPZ** at 180 °C using a microwave reactor (see SI for experimental details). Nanoparticle tracking analysis (NTA) revealed that the resulting g-Odots had an average diameter of 140 nm and exhibited a narrow polydispersity index (PDI) of 0.098 (Fig. 4a). This well-defined size distribution indicates good colloidal stability and is favorable for efficient cellular uptake.

Next, the photophysical properties of the g-Odots were evaluated in aqueous media. As shown in Fig. 4b, **DPPZ**-doped g-Odots exhibited deep red emission with a λ_{em} at 694 nm and a high Φ_{PL} of 40.1%. To the best of our knowledge, this represents the highest quantum yield reported to date for red/NIR g-Odots. Furthermore, time-resolved photoluminescence measurements revealed a long-delayed emission lifetime τ_d of up to 225.5 μs (Fig. 4c), confirming the TADF behavior of the encapsulated luminophore in the nanoparticle system.

Encouraged by the high Φ_{PL} and favorable photophysical properties, the potential of these g-Odots for cellular imaging was further explored. Cell viability assays were first conducted to assess their biocompatibility. As shown in Fig. S7, increasing concentrations of g-Odots had negligible impact on cell viability, indicating excellent biocompatibility. Based on these results, a concentration of 1×10^7 particles per mL was selected for subsequent bioimaging studies. HeLa cells were incubated with the g-Odots suspended in serum-free Dulbecco's Modified Eagle Medium for 2 h, along with Lysotracker Blue DND-22 (100 nM), to evaluate subcellular localization. Confocal microscopy images (Fig. 4d) revealed substantial colocalization of the g-Odots with lysosomes, with a Pearson correlation coefficient of 0.604, suggesting efficient lysosomal targeting.

Time-dependent cellular imaging was also investigated by varying the incubation time of g-Odots. As shown in Fig. S8, increasing the incubation time of **DPPZ** g-Odots had a negligible effect on imaging performance, except for some aggregation observed at longer durations.

Conclusions

In conclusion, we have developed a D–A type NIR TADF emitter, **DPPZ**, exhibiting high quantum yield and favorable excited-state dynamics, and have successfully demonstrated its applicability for NIR bioimaging with lysosomal targeting. In degassed toluene, **DPPZ** displayed a high Φ_{PL} of 54.4%, a maximum emission wavelength at 724 nm, a ΔE_{ST} of 0.26 eV, and a τ_d of 147.8 μs. When doped into a PMMA film (1 wt%), **DPPZ** retained strong TADF characteristics, with a Φ_{PL} of 43.9%, ΔE_{ST} of 0.20 eV, and an extended delayed lifetime of 208.3 μs.

To enable bioimaging applications, water-dispersible g-Odots were fabricated by encapsulating **DPPZ** with the mCP host in the amphiphilic polymer DSPE-PEG2k. The resulting g-Odots exhibited bright red emission with a peak at 694 nm, a high Φ_{PL} of 40.1%, and a long-delayed lifetime of 225.5 μs in aqueous media, representing a rare example of efficient NIR TADF emission in water-dispersible nanostructures. Furthermore, these g-Odots were successfully employed as fluorescent probes for live-cell imaging in HeLa cells, demonstrating good lysosomal targeting and compatibility with single-photon excitation confocal microscopy. This work highlights the promise of D–A-based NIR TADF materials for advanced bioimaging applications.

Conflicts of interest

There are no conflicts to declare.

Data availability

The data supporting this article have been included as part of the supporting information (SI). Supplementary information: Additional synthetic schemes, general experimental considerations, and additional characterization data related to photophysical, thermal, electrochemical, density functional theory, nanoparticle, cell culture. See DOI: **https://doi.org/10.1039/d5tb01740h**.

Spectra and additional information on chemical synthesis are available *via* the Chemotion repository: **https://doi.org/10.14272/reaction/SA-FUHFF-UHFFFADPSC-XNNWJYCHZI-UHFFFADPSC-NUHFF-NUHFF-NUHFF-ZZZ**. Spectra and additional information on the analysis of the target compound is available *via* the Chemotion repository: **https://doi.org/10.14272/XNNWJYCHZINNFI-UHFFFAOYSA-N.1**, **https://dx.doi.org/10.14272/collection/AJ_2025-07-26**.

Acknowledgements

The authors thank the Natural Sciences and Engineering Research Council of Canada (NSERC), the Canada Foundation for Innovation (CFI), and the British Columbia Knowledge Development Fund (BCKDF) for financial support. The authors acknowledge support by the state of Baden-Württemberg through bwHPC and the German Research Foundation (DFG) through grant no. INST 40/575-1 FUGG (JUSTUS 2 cluster). A. S.-P. thanks UBC for an Agnes and Gilbert Hooley Scholarship and for a Miguel A. Romero Sanchez Memorial Fellowship. P. H. thanks UBC for a Four-Year Doctoral Fellowship. S. B. acknowledges the support provided by the Deutsche Forschungsgemeinschaft (DFG) under Germany's Excellence Strategy – 3DMM2O – EXC-2082/1–390761711. Z. M. H. is grateful for a Killam Research Accelerator Fellowship and a Canada Research Chair. The authors gratefully acknowledge support from the UBC Chemistry Biological Services Laboratory and the Life Sciences Institute Imaging Core Facility (RRID:SCR_023783) during this project.

References

1 Q. Sha, X. Li, X. Gu, T. Yuan and J. Hua, *Talanta*, 2025, **286**, 127570.
2 S. Xu, Q. Zhang, X. Han, Y. Wang, X. Wang, M. Nazare, J.-D. Jiang and H.-Y. Hu, *ACS Sens.*, 2020, **5**, 1650–1656.
3 X. Li, G. Baryshnikov, C. Deng, X. Bao, B. Wu, Y. Zhou, H. Ågren and L. Zhu, *Nat. Commun.*, 2019, **10**, 731.
4 J. Jin, H. Jiang, Q. Yang, L. Tang, Y. Tao, Y. Li, R. Chen, C. Zheng, Q. Fan, K. Y. Zhang, Q. Zhao and W. Huang, *Nat. Commun.*, 2020, **11**, 842.
5 Q. Zhang, S. Xu, M. Li, Y. Wang, N. Zhang, Y. Guan, M. Chen, C.-F. Chen and H.-Y. Hu, *Chem. Commun.*, 2019, **55**, 5639–5642.
6 Z. Zhu, D. Tian, P. Gao, K. Wang, Y. Li, X. Shu, J. Zhu and Q. Zhao, *J. Am. Chem. Soc.*, 2018, **140**, 17484–17491.
7 F. Ni, Z. Zhu, X. Tong, W. Zeng, K. An, D. Wei, S. Gong, Q. Zhao, X. Zhou and C. Yang, *Adv. Sci.*, 2019, **6**, 1801729.
8 J. R. Caine, P. Hu, A. T. Gogoulis and Z. M. Hudson, *Acc. Mater. Res.*, 2023, **4**, 879–891.
9 H. Uoyama, K. Goushi, K. Shizu, H. Nomura and C. Adachi, *Nature*, 2012, **492**, 234–238.
10 J. M. Dos Santos, D. Hall, B. Basumatary, M. Bryden, D. Chen, P. Choudhary, T. Comerford, E. Crovini, A. Danos, J. De, S. Diesing, M. Fatahi, M. Griffin, A. K. Gupta, H. Hafeez, L. Hämmerling, E. Hanover, J. Haug, T. Heil, D. Karthik, S. Kumar, O. Lee, H. Li, F. Lucas, C. F. R. Mackenzie, A. Mariko, T. Matulaitis, F. Millward, Y. Olivier, Q. Qi, I. D. W. Samuel, N. Sharma, C. Si, L. Spierling, P. Sudhakar, D. Sun, E. Tankelevičiūtė, M. Duarte Tonet, J. Wang, T. Wang, S. Wu, Y. Xu, L. Zhang and E. Zysman-Colman, *Chem. Rev.*, 2024, **124**, 13736–14110.
11 V. Ferraro, C. Bizzarri and S. Bräse, *Adv. Sci.*, 2024, **11**, 2404866.
12 T. Li, D. Yang, L. Zhai, S. Wang, B. Zhao, N. Fu, L. Wang, Y. Tao and W. Huang, *Adv. Sci.*, 2017, **4**, 1600166.
13 X. Xiong, F. Song, J. Wang, Y. Zhang, Y. Xue, L. Sun, N. Jiang, P. Gao, L. Tian and X. Peng, *J. Am. Chem. Soc.*, 2014, **136**, 9590–9597.
14 W. Hu, L. Guo, L. Bai, X. Miao, Y. Ni, Q. Wang, H. Zhao, M. Xie, L. Li, X. Lu, W. Huang and Q. Fan, *Adv. Healthcare Mater.*, 2018, **7**, 1800299.
15 M. Luo, X. Li, L. Ding, G. Baryshnikov, S. Shen, M. Zhu, L. Zhou, M. Zhang, J. Lu, H. Ågren, X.-D. Wang and L. Zhu, *Angew. Chem., Int. Ed.*, 2020, **59**, 17018–17025.
16 M. Yu, W. Zhao, F. Ni, Q. Zhao and C. Yang, *Adv. Opt. Mater.*, 2022, **10**, 2102437.
17 A. M. Smith, M. C. Mancini and S. Nie, *Nat. Nanotechnol.*, 2009, **4**, 710–711.
18 C. J. Christopherson, N. R. Paisley, Z. Xiao, W. R. Algar and Z. M. Hudson, *J. Am. Chem. Soc.*, 2021, **143**, 13342–13349.

19 Z. Zhu, Z. Luo, Y.-Q. Xie, Y. Sun, L. Xu and Q. Wu, *Adv. Funct. Mater.*, 2024, **34**, 2313701.
20 S. Qi, S. Kim, V.-N. Nguyen, Y. Kim, G. Niu, G. Kim, S.-J. Kim, S. Park and J. Yoon, *ACS Appl. Mater. Interfaces*, 2020, **12**, 51293–51301.
21 J. Zhang, F. Fang, B. Liu, J.-H. Tan, W.-C. Chen, Z. Zhu, Y. Yuan, Y. Wan, X. Cui, S. Li, Q.-X. Tong, J. Zhao, X.-M. Meng and C.-S. Lee, *ACS Appl. Mater. Interfaces*, 2019, **11**, 41051–41061.
22 Y.-F. Xiao, J.-X. Chen, S. Li, W.-W. Tao, S. Tian, K. Wang, X. Cui, Z. Huang, X.-H. Zhang and C.-S. Lee, *Chem. Sci.*, 2020, **11**, 888–895.
23 F. Fang, Y. Yuan, Y. Wan, J. Li, Y. Song, W.-C. Chen, D. Zhao, Y. Chi, M. Li, C.-S. Lee and J. Zhang, *Small*, 2022, **18**, 2106215.
24 Z. Liu, F. Song, W. Shi, G. Gurzadyan, H. Yin, B. Song, R. Liang and X. Peng, *ACS Appl. Mater. Interfaces*, 2019, **11**, 15426–15435.
25 F. Fang, L. Zhu, M. Li, Y. Song, M. Sun, D. Zhao and J. Zhang, *Adv. Sci.*, 2021, **8**, 2102970.
26 Y. Tsuchiya, K. Ikesue, H. Nakanotani and C. Adachi, *Chem. Commun.*, 2019, **55**, 5215–5218.
27 W. L. Primrose, A. Sevilla-Pym and Z. M. Hudson, *Chem. – Eur. J.*, 2025, **31**, e202403399.
28 D. M. Mayder, C. J. Christopherson, W. L. Primrose, A. S. M. Lin and Z. M. Hudson, *J. Mater. Chem. B*, 2022, **10**, 6496–6506.
29 D. M. Mayder, R. Hojo, W. L. Primrose, C. M. Tonge and Z. M. Hudson, *Adv. Funct. Mater.*, 2022, **32**, 2204087.
30 C. Si, W. L. Primrose, Y. Xu, Z. M. Hudson and E. Zysman-Colman, *Adv. Opt. Mater.*, 2025, **13**, 2402576.
31 T. R. Masvikeni, W. L. Primrose, S. Mikulin and Z. M. Hudson, *ACS Appl. Nano Mater.*, 2025, **8**, 11856–11864.
32 J. Xu, Y. Dai, J. Zhang, Z. Jia, Q. Meng and J. Qiao, *Adv. Opt. Mater.*, 2024, **12**, 2300989.
33 Y. Tsuchiya, S. Diesing, F. Bencheikh, Y. Wada, P. L. dos Santos, H. Kaji, E. Zysman-Colman, I. D. W. Samuel and C. Adachi, *J. Phys. Chem. A*, 2021, **125**, 8074–8089.

